The Cousa objective: a long working distance air objective for multiphoton imaging *in vivo*

CHE-HANG YU,[1,*] YIYI YU,[1], LIAM M. ADSIT[2], JEREMY T. CHANG[3], JAD BARCHINI[3], ANDREW H. MOBERLY[4], HADAS BENISTY[4], JINKYUNG KIM[5], ANTHONY J. RICCI[5,6], DAVID FITZPATRICK[3], JESSICA A. CARDIN[4], MICHAEL J. HIGLEY[4], GORDON B. SMITH[7], KRISTINA J. NIELSEN[8], IKUKO T. SMITH[2,9,10] AND SPENCER LAVERE SMITH[1,10,*]

[1]*Department of Electrical and Computer Engineering, University of California Santa Barbara, Santa Barbara, CA 93106, USA*
[2]*Department of Molecular, Cellular, and Developmental Biology, University of California Santa Barbara, Santa Barbara, CA 93106, USA*
[3]*Max Planck Florida Institute for Neuroscience, Jupiter, FL 33458, USA*
[4]*Department of Neuroscience, Yale University, New Haven, CT 06511, USA*
[5]*Department of Otolaryngology, Stanford University School of Medicine, Stanford University, Stanford, CA 94305, USA*
[6]*Department of Molecular and Cellular Physiology, Stanford University School of Medicine, Stanford University, Stanford, CA 94305, USA*
[7]*Department of Neuroscience, University of Minnesota, Minneapolis, MN 55455*
[8]*Solomon H. Snyder Department of Neuroscience, Johns Hopkins University School of Medicine, Baltimore, MD 21205, USA and Zanvyl Krieger Mind/Brain Institute, Johns Hopkins University, Baltimore, MD 21218, USA*
[9]*Department of Psychology and Brain Sciences, University of California Santa Barbara, Santa Barbara, CA 93106, USA*
[10]*Neuroscience Research Institute, University of California Santa Barbara, Santa Barbara, CA 93106, USA*
[*]*sls@ucsb.edu or chehangyu@ucsb.edu*

Abstract

Two-photon microscopy can resolve fluorescence dynamics deep in scattering tissue, but applying this technique *in vivo* is limited by short working distance water-immersion objectives. Here we present an ultra long working distance (20 mm) air objective called the Cousa objective. It is optimized for performance across multiphoton imaging wavelengths, offers a >4 mm^2 FOV with submicron lateral resolution, and is compatible with commonly used multiphoton imaging systems. We share the full optical prescription, along with data on real world performance including *in vivo* calcium imaging in a range of species and approaches.

1. Introduction

Two-photon microscopy of *in vivo* neuronal activity in larger animals, such as monkeys and ferrets, has been challenging due to the mechanical limitations of conventional multiphoton objectives [1–5]. Commercially available microscope objectives with good multiphoton performance often have short working distances (1-10 mm) and/or require water immersion. The short working distance, coupled with the geometry of the objective tip, requires excessive tissue removal and a large cranial window. Such large windows cannot be easily centered over regions of interest, and can exacerbate immune responses and degrade tissue clarity, ultimately limiting the imaging depth and the duration of longitudinal imaging. Water immersion can require awkward reservoirs or the use of gels that can lack appropriate refractive indices and harbor air bubbles that degrade image quality.

To address these issues, we designed an air immersion objective with a working distance of 20 mm, named the Cousa objective. The optics are designed to minimize aberrations for

two-photon imaging. The objective has a numerical aperture (**NA**) of 0.50, which supports submicron lateral resolution imaging. The objective provides diffraction-limited performance over a >4 mm^2 field-of-view (**FOV**). The Cousa objective was designed to be compatible with commercial two-photon imaging systems, with standard threading and an entrance pupil of ∅20 mm. The Cousa objective enables a range of experiments in various species, using commercial off-the-shelf imaging systems.

2. Design

2.1. Specifications and constrains

The design specifications of the 20 mm long working distance objective (**Table 1**) are set and balanced primarily around three factors: *(i)* geometric parameters to facilitate use in animal imaging applications, *(ii)* optimization for two-photon imaging across a large FOV with sub-cellular resolving power, and *(iii)* compatibility with commercial two-photon imaging systems.

First, a top priority of the design, its *raison d'être*, is compatibility with animal experiments and the associated instrumentation. Two-photon imaging in neuroscience is often performed through a cranial window. The objective is then positioned above the window, at a distance determined by the working distance of the objective. This arrangement can pose constraints on imaging. For example, ferrets and other animals have skulls that are > 1 mm thick with a significant gap between the skull and dura mater. In these cases, cranial windows must be enlarged to accommodate standard two-photon objectives, due to their short working distances and tip geometries. Such large imaging windows create challenges for window positioning, imaging quality, and long-term maintenance. For additional examples, even in smaller animals such as mice, short working distances prevent the insertion of auxiliary optics between the objective and sample, and can also prevent imaging in complex preparations such as ventral access to the cochlea.

To address these issues, we started with the requirement that the working distance would be long, 20 mm. By using a long working distance design, the objective can remain comfortably outside of an imaging chamber, resulting in fewer mechanical constraints. We also recognized that imaging at angles other than the conventional vertical orientation, in particular in larger animals, can make maintaining water immersion difficult. Thus, for this design we chose to use air immersion. Air immersion entails a larger refractive index mismatch than water immersion designs, so we mitigated the trade-off by incorporating a correction collar that can compensate for aberrations.

Second, the lens design was optimized for focusing ultrafast laser pulses centered at wavelengths commonly used in two-photon imaging, including popular genetically encoded calcium indicators like the GCaMP series [6–8]. The optics were designed to offer diffraction-limited performance across a range of wavelengths. We set the NA to be 0.50, corresponding to a diffraction-limited resolution of 0.69 μm laterally and 5.84 μm axially, which is sufficient to resolve neurons, dendritic spines, and axonal boutons [9, 10].

Third, the objective was designed to be compatible with commercial multiphoton imaging systems. Major microscope manufacturers use infinity conjugate (i.e., infinity-corrected) optical designs [11], and thus we adopted the same convention for compatibility. The other main constraints from commercial two-photon imaging systems are the beam diameter at the objective back aperture and the maximal scan angle. These parameters are determined by the scan engine. Many commercial two-photon imaging systems constrain the maximal beam diameter to about 20 mm, and the scan angles to about ±3°. We adopted these commonly attained values as design specifications. In addition, we adopted the M32 x 0.75 thread size, which is used on many multiphoton imaging objectives, and thus adapters are readily available.

With these specifications and constraints set (working distance, air immersion, numerical

Working distance*	20 mm
Immersion media*	Air
Numerical aperture*	0.50
Effective focal length*	20 mm
Magnification	10 X *(with a 200 mm focal length tube lens)*
Correction collar*	0 - 1 mm cover glass thickness
Entrance pupil*	20 mm
Scanning angles*	±3°
Field of view (FOV)	2.08 mm
Primary wavelength range*	920 nm ± 10 nm
Full wavelength range	800 - 1300 nm
Anti-reflective coating	< 0.5% reflected 450-1100 nm *(per surface)*
Parfocal distance	~ 90 mm
Mounting threads*	M32 x 0.75
Weight	477 g
Group delay dispersion	~4910 fs^2 at 920 nm

Table 1. Specifications of the long working distance air objective. Parameters that were used to constrain the initial design are marked with an asterisk (*).

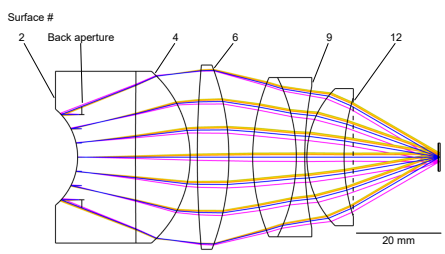

Surface #	Description	Radius (mm)	Thickness (mm)	Material	Semi-Diameter	Mech Semi-Dia
OBJECT		Inf	Inf			
Stop	Back aperture	Inf	-1.000		10	10
2		-14.773	13.669	S-LAH58	11.27	20.155
3		1572.581	12.899	S-LAL21	18.118	20.155
4		-26.775	1.692		20.155	20.155
5		240.655	7.464	S-LAH59	21.497	21.619
6	Adjustable gap	-60.321	5.621		21.619	21.619
7		47.162	10.302	S-FPM2	18.679	18.679
8		-41.597	1.999	S-NPH3	18.679	18.679
9		84.414	0.5		16.643	18.679
10		22.719	8.777	S-LAH58	16.090	16.090
11		45.328	2.194		13.93	16.090
12	Working distance	Inf	20.006		13.752	13.752
13	Coverslip	Inf	0.17	BK-7	3.30	3.30
14		Inf	0.35	SEAWATER	3.30	3.30
15	Image plane	Inf		SEAWATER	3.30	3.30

Fig. 1. Lens layout and prescription. The maximal scan field is ±3°, and the effective focal length is 20 mm. The adjustable air gap is set at the thickness of Surface 6 to implement the function of a correction collar. The working distance, which is 20 mm, is the air space between the objective tip (Surface 12, dashed line) to the surface of the coverslip glass (Surface 13). The optimization routines were set assuming a focal plane ~ 0.35 mm into the brain, as indicated on the prescription (Surface 14).

aperture, scan angle, and back aperture diameter), a relatively large FOV remains feasible by setting the effective focal length of the objective to 20 mm [12]. The design and optimization process was conducted using optical simulation software (ZEMAX OpticStudio). The merit

function prioritized maximizing the working distance while maintaining a diffraction-limited point spread function and minimizing the wavefront error across the FOV. Parallel efforts were made to reduce the number of lenses and the thickness of the materials, and thus minimize the size, weight, and cost of the final design.

2.2. Design and model performance

The infinity corrected objective consists of six lens elements (**Fig. 1**) with a net group delay dispersion of ~4910 fs^2 at 920 nm [13]. The working distance (surface 12 to the focal plane at surface 15) is ~20 mm. The position of the back aperture was designed to be very close to the first element, surface 2. This facilitates alignment in commercial systems, since visual inspection at the back surface can determine whether the excitation beam remains stationary during scanning. In the model, the root-mean-square (**RMS**) wavefront error for 920±10 nm light is less than 0.02λ across the scan angles, which is considerably less than the diffraction limit of 0.072λ (**Fig. 2a**). Similarly, the Strehl ratio [14] is over 0.97 across the nominal ±3° scan angles (**Fig. 2b**), exceeding the diffraction limit of 0.8. Thus the performance is diffraction-limited throughout the designed FOV by a large margin. This margin provides some assurance that performance will remain diffraction-limited despite real-world imperfections that are incorporated during fabrication and assembly.

The objective has an air gap between surfaces 6 and 7 that is adjusted by a rotating correction collar. Correction collar adjustments can compensate for a range of cover glass (surface 13) thicknesses, from 0 to 1.0 mm. The correction collar can also be adjusted to optimize performance at different excitation wavelengths (**Fig. 2**). Adjusting two free parameters, the precise focal plane location and the correction collar position, diffraction-limited performance can be extended to a range of 800-1300 nm for multiphoton excitation at a range of wavelengths (**Fig. 2c, 2d, and Table 2**). Note that the refocusing is applied at a single position for all scan angles, and the merit function balances performance over the full FOV.

Refocus by adjusting objective-sample air gap (surface 12)*											
Wavelengths (nm)	800	850	900	950	1000	1050	1100	1150	1200	1250	1300
Air gap at surface 12 (mm)	20.018	20.009	20.006	20.007	20.011	20.018	20.027	20.038	20.05	20.065	20.08
*Thickness of surface 6 = 5.621 mm; Coverslip thickness = 0.17mm											
Refocus by adjusting objective-sample air gap (surface 12) and correction collar (surface 6)**											
Wavelengths (nm)	800	850	900	950	1000	1050	1100	1150	1200	1250	1300
Air gap at surface 12 (mm)	20.011	20.006	20.005	20.007	20.012	20.018	20.026	20.035	20.046	20.057	20.07
Air gap at surface 6 (mm)	5.669	5.643	5.626	5.618	5.615	5.619	5.627	5.639	5.656	5.675	5.699
**Coverslip thickness = 0.17mm											

Table 2. The nominal thicknesses of air gaps used for different wavelengths. The upper portion of table lists the distance of the objective-to-sample gap (Surface 12) when this single air gap is adjusted for different wavelengths. The lower part of the table shows the thicknesses of the objective-to-sample gap (Surface 12) and the correction collar gap (Surface 6) when both of these two air gaps are adjusted.

2.3. Mechanical model and assembly

After optical designs were finalized, the mechanical design, lens fabrication, housing manufacturing, and objective assembly processes were contracted to an external firm (Special Optics, Denville, NJ, USA). The objective is 79 mm long and 65 mm wide, and the total weight is 477 grams (**Fig. 3**). The long working distance of the objective relaxes the geometric constraints of the design, as was our strategy. However, one mechanical constraint remained: the objective needed to fit within the clearance around the objective mounting threads of commonly used multiphoton microscopes. A conventional way to load the optics into an objective is to leave the back open, insert all lenses, and then seal it off. This stacking approach leads to the largest

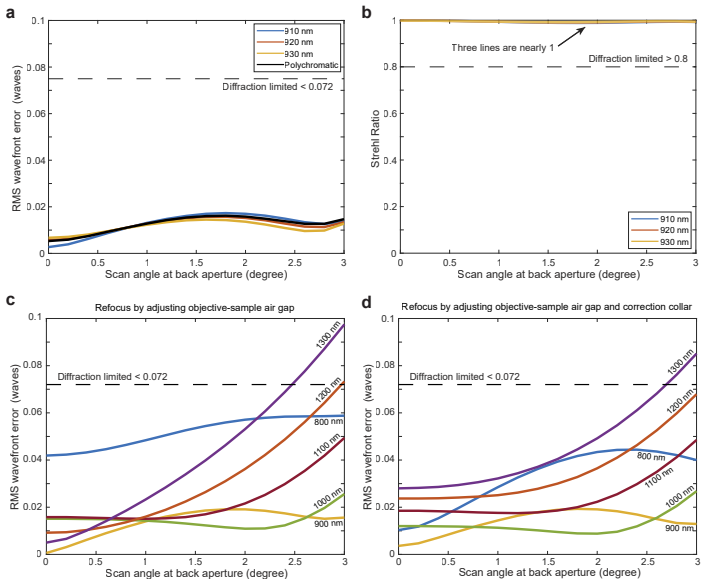

Fig. 2. Performance analysis. The primary optimizations were for 920 ± 10 nm, for two-photon excitation of green fluorescent protein (GFP)-based indicators with ultrafast pulses of light. The optical model predicts (a) low root-mean-squared (RMS) wavefront errors and (b) high Strehl ratios for 910 nm, 920 nm, and 930 nm light across the scan angles of 0 - 3°. This shows a large degree of optimization, well beyond the diffraction limit, for this primary wavelength window. (c) Performance is also diffraction-limited across a broader wavelength range from 800 - 1300 nm. The longest wavelengths, 1200 nm and 1300 nm will likely be somewhat vignetted (have higher aberrations) only at the very edge of the FOV. The RMS wavefront error remains below the diffraction limit for most of the 0 - 3° scan angle range, when the focal plane is allowed to naturally shift with wavelength. (d) The correction collar provides an additional degree of optimization. Using both parameters (adjusting the correction collar and allowing for refocusing with wavelength), the RMS wavefront error remains below the diffraction-limit for an even larger extent of the scan range for the 1200 nm and 1300 nm light. Note that this optimization increases RMS wavefront error at small scan angles, as a trade-off for a reduction at higher angles. Still, the performance remains below the diffraction limit (0.072λ). Overall, a diffraction-limited performance is attained across a broad range of wavelengths, and across a wide FOV.

diameters being at the back of the objective, near the threads. Realizing this problem in an early version, we redesigned the optomechanics for assembly in the middle, at the adjustable air gap surface (Surface 6). Lenses are loaded from this plane, into both halves, and then the two halves are joined. This reduced the diameter of the shoulder near the threads, and moved the largest diameter to the middle of the lens, where it can be more easily accommodated on commercial multiphoton microscopes. The resulting silhouette of the objective resembles a cousa squash, and inspired the name of the objective (**Fig. 3a**). The total traveling range of the adjustable air gap is 1.0 mm, corresponding to 1.3 revolutions of the correction collar, with a precision of 2.08 μm per degree. The correction collar is marked to indicate both 360-degrees around the objective, and various cover glass thicknesses. The tip of the objective is beveled at 45° to gain some clearance near the sample space.

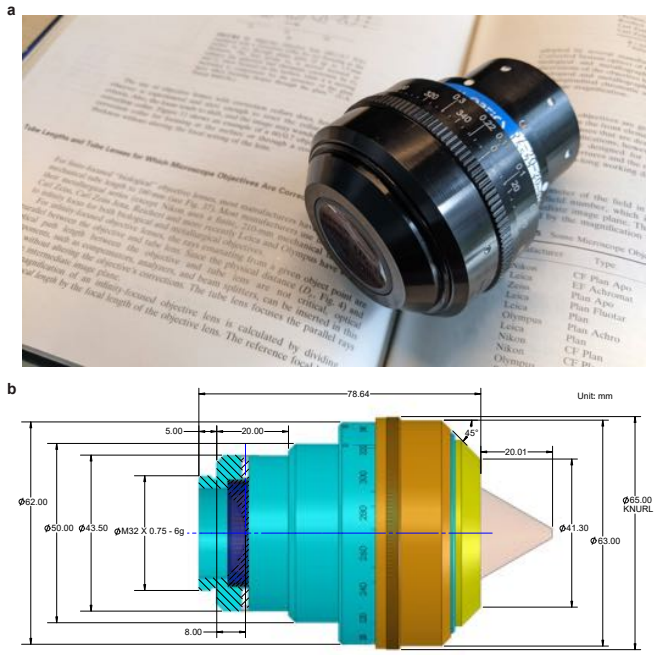

Fig. 3. The housing of the objective. (a) A photograph of the manufactured objective, and (b) the mechanical model of the objective. All dimensions are in mm unless otherwise noted.

3. Characterization and performance

3.1. Resolution, field-of-view, and light transmission

We characterized the real world performance of the objective using a custom two-photon scan engine with a 32 mm diameter beam scanned over a ±5° range [9]. These scan parameters exceed the requirements of the objective (20 mm and ±3°, respectively), thus the performance should be objective-limited, rather than scan engine-limited. We first measured the resolution attained by the objective by taking z-stacks of 0.2 μm fluorescent beads at various positions across the FOV (**Fig. 4a and 4b**). The lateral FWHM is 0.69 μm throughout the FOV, which is consistent with the theoretical diffraction-limited resolution [15]. The axial resolution is 5.84 μm, again providing a good match to the theoretical value, up to ±2° scan angles, and deviates by about 10% at 3° of scan angle. The match between the experimental measurement and the theoretical calculation confirms that the NA of the objective is 0.50, as designed. This result also implies that the RMS wavefront error is low.

We next measured the imaging FOV with a structured fluorescent sample with periodic lines (5 per mm; item 57–905, Edmund Optics). When the scan angle is ±3°, the images contain 10 lines along both the x and y directions without vignetting, indicating a 2 mm length on each axis of the FOV (**Fig. 4c**). The result demonstrates that the objective has a FOV of 2 × 2 mm^2 area, consistent with the nominal model performance (**Fig. 2**). The FOV can be extended to ~3 x 3 mm^2 with a scan of ±5°, and vignetting occurs at the corners of the field (**Fig. 4c**).

The broadband antireflective coating applied to the lenses was measured to transmit on average 99.5% of visible and near-infrared light (450 - 1100 nm) per surface. To measure the total transmission of 910 nm and 532 nm light through this objective, we supplied an under-filling laser beam into the objective, and measured its power before and after the objective. We found that 86% of 910 nm and 91% of 532 nm light were transmitted through the objective, showing

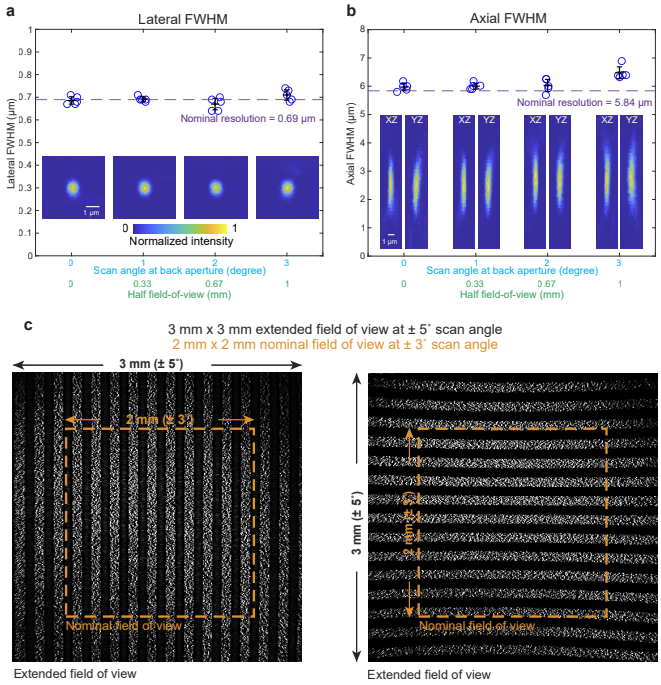

Fig. 4. Characterization of the resolution and FOV. Two-photon excitation PSF measurements were made with 0.2-μm beads embedded in agar at a depth of 350 μm covered by 170-μm thick coverslip. Z-stack images are acquired for beads at four lateral locations including on-axis, 1°, 2°, and 3° off-axis. Full-width at half-maximum (FWHM) of the Gaussian fits for measurements from the fluorescence beads laterally (a) and axially (b) are calculated and plotted. Five beads (n=5) at each locations are measured. Data are presented as mean values±S.D. Dashed lines in (a) and (b) indicates the theoretical lateral and axial FWHM , respectively. Insets in (a) and (b) show the example images of the XY, XZ, and YZ cross-sections of the measured beads at each scan angle. (c) XY images of a fluorescent calibration sample with a periodic line pattern (5 lines per millimeter) in two orientations acquired under a ±5° scan angle. Each image shows 15 lines on the top edge (left image) and on the left edge (right image), receptively, corresponding to a 3 × 3 mm FOV. Both the dashed squares show a nominal 2 x 2 mm FOV of the objective under the ±3° scan angle.

very high transmission throughput at both the excitation and emission wavelengths for green fluorescence protein imaging.

3.2. In vivo two-photon calcium imaging in mouse

After benchmarking the optical performance of the objective, we tested the performance in the target application: two-photon imaging *in vivo*. The Cousa objective was used on a range of multiphoton imaging systems, including custom-built systems and commercial systems from Bruker, Thorlabs, Neurolabware, and Sutter. Three different animal species were used as well: mouse, ferret, and tree shrew.

As a first test, a cranial window was implanted in a transgenic mouse with neurons expressing the genetically encoded calcium indicator GCaMP6s [16]. The Cousa objective was mounted on a custom microscope that provided a ±2.6° scan angle range and a 20 mm diameter beam at the back aperture of the objective. This system also had a 12 kHz resonant scanner for fast

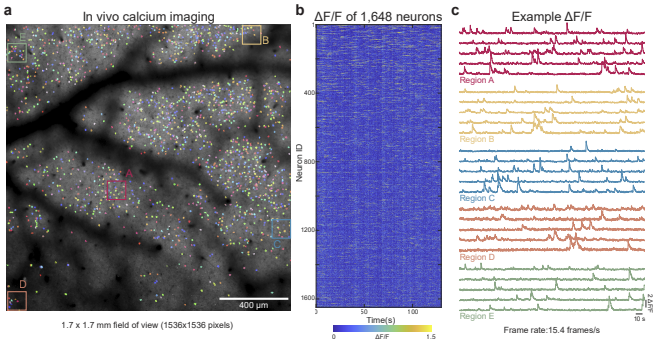

Fig. 5. *In vivo* calcium imaging. (a) Calcium indicator dynamics were imaged *in vivo* over a 1.7 x 1.7 mm FOV through a cranial window on a transgenic mouse expressing the genetically encoded fluorescent calcium indicator GCaMP6s in excitatory neurons. The color-coded regions are neurons with calcium activity identified. (b) Calcium transients (ΔF/F) from 1648 neurons were detected and plotted over time. (c) Examples of ΔF/F from different regions in (a) are plotted.

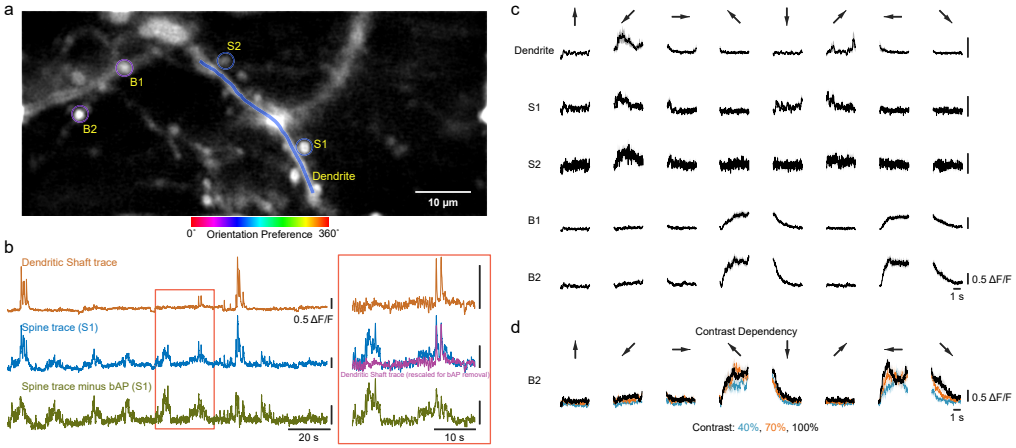

Fig. 6. *In vivo* imaging of neural processes and orientation tuning in mice. (a) *In vivo* calcium transients from neural processes were recorded through a cranial window in a mouse with ultra-sparse expression of GCaMP8m in V1. Black and white drifting gratings were presented on a display monocularly. Putative axonal boutons (B), dendritic spines (S), and dendritic shafts were clearly resolved. Color-codes show the orientation preference of each region of interest. (b) Calcium transients from the dendrite (brown) and the dendritic spine S1 before back-propagating action potential (bAP) signal is removed (blue). After the bAP signal was removed, the trace of spine S1 (green) shows many activity events that are independent from its local dendritic shaft. *(inset)* An expanded view shows further details the subtraction procedure, including a rescaled trace from the dendritic shaft (purple) for removal of the bAP signals. (c) Orientation tuned responses for were reliable for spines S1 and S2, boutons B1 and B2, and the nearby dendrite (n = 15 repeats per stimulus; mean in black ± SEM in gray). (d) Responses in axonal bouton B2 varied with contrast (contrast levels of 40% in blue, 70% in orange, and 100% in black. Traces show the mean ± SEM in shading; n = 5 repeats for each contrast and orientation).

raster scanning. First, a z-stack image series was acquired covering the volume of 1 x 1 x 0.5 mm^3 (X*Y*Z) (**Video 1**). This data demonstrated that individual neurons were resolved up to the depth of 0.5 mm. Next, a FOV of 1.7 x 1.7 mm^2 was recorded using the full ±2.6° scan angle at back aperture (**Fig. 5a, Video 2**) with 1536 scan lines, 1536 pixels per scan line, and a frame rate of 15.4 frames/s. Spontaneous calcium transients were imaged from 1648 neurons detected throughout the FOV (**Fig. 5b**). Calcium indicator traces from neurons across the FOV exhibited high ΔF/F signals (**Fig. 5c**). These *in vivo* results demonstrate performance in the target application, with a relatively large FOV, even when using relatively short pixel dwell times (∼28 ns / pixel or ∼2 pulses / pixel).

We next performed two-photon imaging of dendrites and axons in a mouse that sparsely expressed GCaMP8m. Neuronal activity in the primary visual cortex (**V1**) was imaged while the animal viewed black and white drifting gratings of eight different orientations (0-315° and 45° steps). The spines and their local dendritic shaft are clearly resolved, and some putative boutons are identified with distinctive calcium activity (**Fig. 6a**). Dendritic spine transients showed clear independent calcium dynamics in addition to those associated with back-propagating action potentials (**bAP**), demonstrating that the fluorescence signals from the spine and its parent dendrites can be unambiguously extracted such that the bAP signals can be removed from the spine with high fidelity (**Fig. 6b**) [6]. These identified spines, boutons, and dendrite show reliable response to visual stimuli and different orientation tuning (**Fig. 6c**). Moreover, response magnitude of the axonal bouton transients showed contrast-dependence (40%, 70%, and 100%), further highlighting the sensitivity of the objective and performance in challenging experiments (**Fig. 6d**). Taken together, these results demonstrate that the Cousa objective has not only high resolution for resolving minute structures in neural processes, but also sufficient two-photon excitation and collection efficiency to detect fine changes in calcium transients.

3.3. In vivo two-photon calcium imaging in ferret and tree shrew

As previously discussed, two-photon microscopy of *in vivo* neuronal activity in larger animals can be challenging due to the mechanical limitation of multiphoton objectives. Therefore, we tested the Cousa objective in ferrets and tree shrews. The objective was mounted on a commercially available microscope (B-Scope; Thorlabs) to image calcium dynamics in neurons in ferret and tree shrew V1. Injected viral particles transduced neurons to express GCaMP6s [16]. For ferret imaging, wide-field imaging was used to image the vasculature and the orientation preference map in V1 (**Fig. 7a**). Then, two-photon imaging through the Cousa objective was used to resolve neuronal activity of individual neurons within a 2 x 2 mm FOV (**Fig. 7b**). Individual neurons exhibited reliable responses to visual stimuli with edges of particular orientations (**Fig. 7c**). Observed two-photon orientation preferences were also consistent with their location within the orientation preference map (as measured with widefield imaging).

In tree shrews, V1 neurons were transduced to express GCaMP6s [16]. The Cousa objective was used to image calcium transients (**Fig. 8a**). Individual neurons could be registered to their location in the local orientation preference map (**Fig. 8b**), and reliable responses to visual stimuli were resolved (**Fig. 8c**). In both ferret and tree shrew V1 imaging, the Cousa objective offered a larger FOV than conventional objectives, and the air immersion increased the reliability of long-term imaging sessions, over which maintenance of a water interface can be unreliable, especially when imaging at and angle. Together, these experiments demonstrate that the Cousa objective supports multiphoton imaging in ferrets and tree shrews.

3.4. Simultaneous 2-photon and mesoscopic widefield imaging in awake, head-fixed mice

Many objectives used in two-photon imaging are designed for water immersion, which can complicate experiments where the objective needs to be held at an angle far from vertical. In

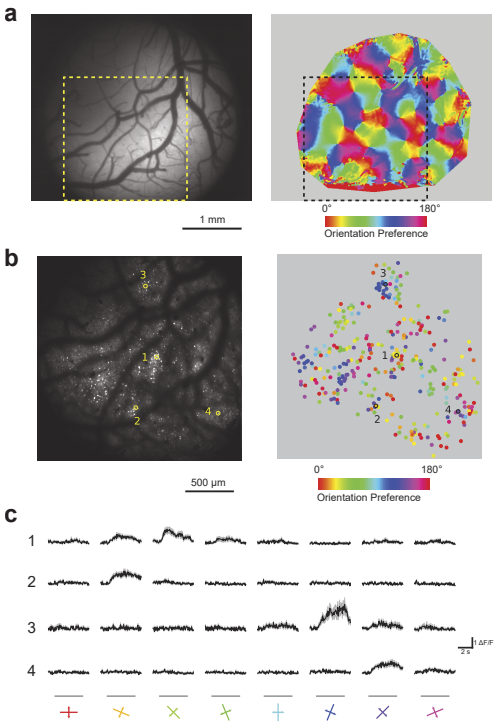

Fig. 7. Orientation preference maps in ferret. (a) Widefield epifluorescence calcium imaging of ferret visual cortex using a 4x objective. FOV (left) and orientation preference map (right). Dashed boxes denote the approximate two-photon FOV shown in (b). (b) Two-photon calcium imaging of the corresponding FOV shown in (a) using the Cousa objective. FOV (left) and scatter of cellular orientation preferences (right). (c) Orientation tuned cellular responses for presentation of oriented stimuli for the four cells shown in (b). Traces show mean (black) and SEM (gray). Horizontal gray bars denote the stimulus presentation period.

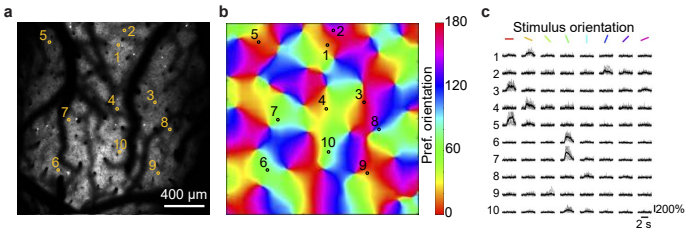

Fig. 8. Orientation preference maps in tree shrew. (a) GCaMP6s expression in a 2x2 mm FOV, 136 μm below the pia in tree shrew V1. Ten example neurons were selected. (b) Pixel-wise orientation preference map generated by two-photon imaging. (c) Orientation tuned cellular responses of the example neurons shown in (a) and (b). Traces show mean (black) and single trials (gray).

addition, short working distances preclude the implementation of intermediate optics between the objective and the sample. Long working distance air objectives can enable experiments such as simultaneous mesoscopic and two-photon imaging of neuronal activity [17]. In this method,

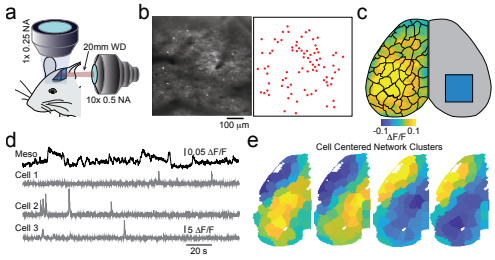

Fig. 9. Dual 2-photon/mesoscopic imaging in awake, head-fixed mice. (a) Schematic illustrating the imaging configuration. Awake, head-fixed mice (n=2) were placed under the objective of a widefield microscope. Cellular data were acquired through the Cousa objective directing the light path through a prism placed over visual cortex. (b) Time-averaged 2-photon FOV (left) and location of imaged neurons (right) for a representative experiment. (c) Example mesoscopic imaging frame with overlaid functional parcellation boundaries. Prism location in opposite hemisphere is indicated. (d) Example time series for three representative neurons and a parcel over the visual cortex. (e) Average k means-clustered (k=4) cell-centered networks for 74 neurons in one animal.

dual asymmetric imaging pathways are used to record the activity of individual neurons relative to ongoing, large-scale dynamics across the dorsal neocortex. The Cousa objective was mounted horizontally and used in conjunction with a micro prism implanted on the cortical surface (**Fig. 9**) [17]. Compared to prior instrumentation, the Cousa objective offered a larger FOV (more neurons imaged) and a higher NA (i.e., improved resolution).

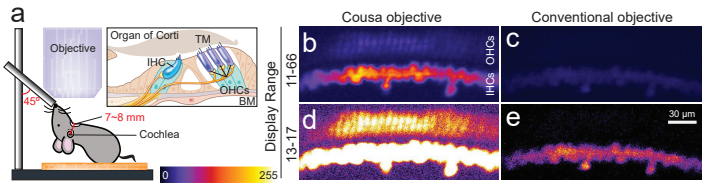

Fig. 10. *In vivo* cochlear hair cell imaging with the Cousa objective and a conventional objective. (a) Illustration of the mouse position for two-photon imaging of the organ of Corti in the cochlea. IHC, inner hair cell; OHC, outer hair cell; TM, tectorial membrane; BM, basilar membrane. The color bar indicates a look-up table with a range of 0-255 for panels b-e. (b-e) Z-projection images of IHCs and OHCs with the Cousa objective or a conventional objective. The display range of 11-66 or 13-17 was applied for comparison of the objectives.

3.5. Imaging the mouse cochlea in vivo

Challenging surgical preparations are another example of experiments requiring challenging imaging angles, ample working distances, air immersion, and optimized two-photon performance. Using *in vivo* multicellular imaging, we can directly measure neuronal responses in peripheral sensory encoding or sight [18], smell [19], taste [20] and touch [21]. However, obtaining similar *in vivo* information in the auditory system is particularly challenging. The peripheral end organ, the cochlea, is difficult to reach surgically and optically. The cochlea is located deep in the temporal bone, next to the bulla, tympanic membrane, and other structures that limit optical access. Moreover, it is a mechanosensitive, fluid-filled structure, which further complicates

surgical preparations and functional imaging. Recently, a novel surgical approach overcame these challenges, enabling *in vivo* visualization of multiple cochlear cells while preserving hearing function [21]. In this approach, a long working distance objective (> 8 mm) is required to keep the neighboring hearing structures intact (**Fig. 10a**). Furthermore, an air objective is needed since an air-filled middle ear cavity is critical for sound transference through the middle ear *in vivo*. Water or oil coupling for the objective interrupts effective sound transfer. However, existing long working distance air objectives with NA (> 0.40) have poor performance (transmission and/or aberration correction) for the near-infrared wavelengths used in two-photon microscopy. Thus, high laser power is required. Here, we directly compare the performance of the Cousa objective with a conventional long working distance objective in this application. Two-photon images of the organ of Corti were collected *in vivo* with the same laser power (30 mW) in a genetically modified mouse (a hair cell-targeted Myosin15Cre line crossed with a TdTomato reporter line). The image intensity of inner and outer hair cells (**IHCs and OHCs**) from the Cousa objective is higher than that from a conventional objective (**Fig. 10b-e**). Specifically, the display range of 11-66 (arbitrary units) visualized both IHCs and OHCs with with the Cousa objective, while with the conventional objective cells were rarely detected (**Fig. 10b,c**). Similarly, the proper display range of 13-17 for the conventional objective made the signal from the Cousa objective saturated (**Fig. 10d,e**). Lastly, doubled laser power (60 mW) for improving image quality with the conventional objective induced cell damage. Taken together, the Cousa objective shows a much greater efficiency for cochlear *in vivo* imaging compared to a conventional objective, thus enabling measurements with less laser power.

4. Discussion

In summary, we developed a new objective optimized to enable new multiphoton experiments. The key attributes of the Cousa objective include a 20 mm working distance, air immersion, an NA of 0.50, and a FOV of 4 mm^2 (up to 9 mm^2 at ± 5° scanning). It is optimized for low aberration imaging across the near infrared (IR) spectrum (800 - 1300 nm) for multiphoton excitation. The Cousa objective is designed to readily integrate with and maximally exploit commercial microscope systems, with its 20 mm diameter back aperture and M32 x 0.75 mounting threads. The lens description is fully open-source, so that the community can readily duplicate, modify, or simulate for their applications. The manufactured objective has been distributed to an array of labs, and their results demonstrate functional and structural two-photon imaging *in vivo*. In conclusion, this ready-to-use open source objective can facilitate a variety of two-photon imaging experiments in a wide range of animals.

5. Methods

5.1. Objective design and assembly

The objective was modeled and optimized using an optical design software of OpticStudio (Zemax, LLC). Tolerance analysis indicated that 90% of the completed objectives would have an RMS wavefront error of 0.048λ (still well below the diffraction limit criterion of 0.072λ) with commonly attained manufacturing and assembly tolerances. All lenses in the objective were manufactured, aligned, and assembled in the factory of Special Optics (Denville, NJ, USA). The manufacturing tolerances used were 0.005 mm total indicator runout (TIR) for decentration and tilt, 0.05 mm for thickness, 4 rings for radius (power), .25 waves at 633 nm for irregularity, 0.005 mm for wedge, 60-40 scratch-dig, and 0.01 arc min for lens decentration.

5.2. In vivo two photon imaging system

All imaging was performed using two custom two-photon systems. One system equipped a 8 kHz resonant scanner (CRS 8 kHz, Cambridge technology) supplies a 32-mm diameter beam

size and ±5° scan angles at the objective back aperture. The detailed information of this system can be found in this reference [9]. The other system equipped a 12 kHz resonant scanner (CRS 12 kHz, Cambridge technology) supplies a higher imaging frame rate with a 20-mm beam size and ±2.6° scan angles at the objective back aperture. Our laser source is a Ti:sapphire pulsed laser with a central wavelength at 910 nm and a 80 MHz repetition rate (Mai-Tai, Newport). The image acquisition were controlled by ScanImage from Vidrio Technologies Inc. The imaging was performed with a power ≤80 mW out of the front of the objective. No damage was observed from the surface of the dura to the 500 μm depth. Assessment of damage due to laser intensity was based on visual morphological changes to the appearance of the dura mater and/or continuously bright cell bodies.

5.3. Excitation point spread function measurements and simulations

The measurement and analysis procedure were described in our previous publication in details [10]. To evaluate the excitation point spread function (PSF), sub-micrometer beads were imaged. Sub-micrometer fluorescent beads (0.2 μm, Invitrogen F-8811) were embedded in a thick (1.2 mm) 0.75% agarose gel. 30 μm z-stacks were acquired, each centered at a depth 250 μm. The stage was moved axially in 0.5 μm increments (Δstage). At each focal plane 30 frames were acquired and averaged to yield a high signal-to-noise image. Due to the difference between the refractive index of the objective immersion medium (air) and the specimen medium (water), the actual focal position within the specimen was moved an amount Δfocus = 1.38 x Δstage [22]. The factor 1.38 was determined in Zemax and slightly differs from the paraxial approximation of 1.33. These z-stack images were imported into MATLAB for analysis. For the axial PSF, XZ and YZ images were created at the center of a bead, and a line plot was made at an angle maximizing the axial intensity spread, thereby preventing underestimation of the PSF due to tilted focal shifts. For the radial PSF, an XY image was found at the maximum intensity position axially. A line scan in X and Y was made. Gaussian curves were fit to the individual line scans to extract FWHM measurements. The radial PSF values are an average of the X PSF and Y PSF, and the axial PSF is an average of the axial PSF found from the XZ and YZ images. Excitation PSF measurements were performed at locations of on axis, 1°, 2°, and 3° off axis across the FOV. Data reported (Fig. 4a and 4b) are the mean ± S.D. of 5 beads (n=5) at each location.

5.4. Animal experiments

5.4.1. Mouse experiments in Figures 5 and 6

All procedures involving living animals were carried out in accordance with the guidelines and regulations of the US Department of Health and Human Services and approved by the Institutional Animal Care and Use Committee at University of California, Santa Barbara. Mice were housed in 12 h dark/light reverse cycle room. The temperature set-point is 74–76 °F; the low-temperature alarm is 70 °F; the high-temperature alarm is 78 °F. The relative humidity is 45% (range 30–70%).

For population calcium imaging, GCaMP6s transgenic mice were used, which were generated by triple crossing of TITL-GCaMP6s mice, Emx1-Cre mice (Jackson Labs stock #005628) and ROSA:LNL:tTA mice (Jackson Labs stock #011008). TITL-GCaMP6s mice were kindly provided by Allen institute. Transgenic mice were deeply anesthetized using isoflurane (1.5–2%) augmented with acepromazine (2 mg/kg body weight) during craniotomy surgery. Carpofen (5 mg/kg body weight) was administered prior to surgery, as well as after surgery for 3 consecutive days. Glass windows were implanted over visual cortex as previously described [9]. Ca^{2+} signals were analyzed using custom software [23] in MATLAB (Mathworks). Neurons were segmented and fluorescence time courses were extracted from imaging stacks using Suite2p (https://suite2p.readthedocs.io/en/latest/) [24]. Signals from neurons are a sum of neuronal and neuropil components. The neuropil component was subtracted from the neuronal signals by

separately detecting it and subtracting it. The neuropil component was isolated using the signal from an annulus region around each neuron, and then subtracted from the neuronal signal to provide a higher fidelity report of neuronal fluorescence dynamics. An exponential moving average with a moving window size of 5 samples (0.32 s) was used to reduce the baseline noise in the traces displayed (**Fig. 5c**).

For dendrite calcium imaging, adult (> 8 weeks) C57Bl/6 mice of both sexes (Jackson Labs) were used. A 4-mm diameter craniotomy was performed over visual cortex as previously described [25]. Briefly, mice were premedicated with a sedative, acepromazine (2 mg/kg body weight, i.p.), after which they were deeply anesthetized using isoflurane (2-3% for induction, 1-1.5% for surgery). The mouse's body temperature was monitored and actively maintained using an electronic heat pad regulated via rectal probe. Carprofen (5 mg/kg body weight, s.c.) was administered preoperatively, and lidocaine solution containing epinephrine (5 mg/kg body weight s.c.) was injected locally before and after the scalp excision. The scalp overlaying the right visual cortex was removed and a custom head-fixing imaging chamber with a 5-mm diameter opening was mounted to the skull with cyanoacrylate-based glue (Oasis Medical) and dental acrylic (Lang Dental). Mice were mounted on a custom holder via the headplate chamber, which was filled with a physiological saline containing (in mM) 150 NaCl, 2.5 KCl, 10 HEPES, 2 CaCl2 and 1 MgCl2. A craniotomy was performed using carbide and diamond dental burs on a contra-angle handpiece (NSK). adeno-associated viral (AAV) vectors were injected in to V1 under continued isoflurane anesthesia as previously described [25–27]. Briefly, 1:1 mixture of pENN.AAV.CamKII 0.4.Cre.SV40(AAV1; Addgene #105558; diluted at 1:20,000 in phosphate buffered saline (PBS)) and pGP.AAV.syn.GLEX.jGCaMP8m.WPRE (AAV1; Addgene #162378; original concentration at $\sim 10^{13}$ vg/mL) viral particles were injected (80 nL per site; 1 site per animal) into V1 with a pulled-glass capillary micropipette using a Nanoliter 2010 controlled by a microprocessor, Micro4 (World Precision Instruments), at 15 nL per min. The glass pipette was left in place for 5 mins before retracting to avoid the backflushing of the injected solution. The cranial window was then sealed with a glass cranial plug made up of 4-mm and 3-mm circular coverslips (Warner Instruments) stacked in tandem with a UV-curing optical adhesive (NOA61, Norland). Two-photon imaging of Ca2+ transients indicated by GCaMP8m was performed starting 4-6 weeks after AAV injection, using a custom-built two-photon microscope used in prior studies [25, 28]. Frame scans were acquired using ScanImage [29] at 58.2 frames per second, 512x256 pixels; 31000 frames total per visual stimulation session.

Visual stimuli were presented on a 7" monitor (60 Hz refresh rate) placed 12 cm away from the animal's eye. To assess orientation tuning of the dendritic shaft, spines, and putative axonal boutons, full field square gratings at 40%, 70%, and 100% contrasts (0.04 cycles per degree at 2 Hz) were presented in 8 directions (0°, 45°, 90°, 135°, 180°, 225°, 270°, 315°) for 5 trials. Each grating drifted for 4 seconds. A notch filter centered at 2 Hz (± 0.5 Hz bandwidth) was used to remove a small amount of light leakage from the stimulus monitor into the imaging pathway.

To functionally map visual cortex for targeted injection of viral vectors, ISOI was performed using a custom macroscope and a CCD camera as previously described [25, 30]. Retinotopic maps were used to locate V1. The pial vasculature map relative to the retinotopic maps was used to guide targeted injections into V1.

5.4.2. Ferret and tree shrew experiments in Figures 7 and 8

All experimental procedures were approved by the Max Planck Florida Institute for Neuroscience Institutional Animal Care and Use committee and were performed in accordance with guidelines from the U.S. National Institute of Health. We used one juvenile female ferret from Marshal Farms and one adult male tree shrew for this study.

Viral transduction and terminal imaging in L2/3 of the anesthetized ferret and tree shrew were performed as previously described [31, 32]. Briefly, we expressed GCaMP6s by direct

microinjection of AAV2/1-hSyn-GCaMP6s-WPRE-SV40 (Addgene, 100843-AAV1, Titer: 2.5^{13} GC/mL) into the visual cortex. Subsequently a cranial window was implanted over visual cortex and imaged. An injection into the visual cortex of the ferret was made at P21, and imaging was performed at P42. Imaging in the tree shrew occurred 16 days after viral transduction.

Two-photon imaging of GCaMP6s was performed with a Bergamo II series microscope (Thorlabs) equipped with an 8 kHz resonant-galvo scanner and driven by a Mai-Tai DeepSee laser or Insight DS+ (Spectra-Physicis) at 910 nm or 920 nm respectively. Average excitation power at the exit of the objective ranged from 40 to 60 mW. The microscope was controlled by ScanImage (MBF Bioscience). Images were acquired at 15 Hz (1024x1024 pixels in the ferret, 512x512 pixels in the tree shrew). Widefield epifluorescence imaging of GCaMP6s in the ferret was achieved with a Zyla 5.5 sCMOS camera (Andor) controlled by μManager [33] through a 4x air-immersion objective (Olympus, UPlanFL 4x N/0.13NA) and images were acquired at 15 Hz with 4x4 binning to yield 640x540 pixel images.

Visual stimuli were presented on an LCD screen using PsychoPy (v1.85) [34]. The monitor (30 cm x 52 cm, 1920 x 1080 pixels, 120 Hz refresh rate) was placed 25 centimeters in front of the animal. To evoke orientation-specific responses, full field square gratings at 100% contrast were presented in 16 directions (8 orientations) for 10 trials (ferret) or 8 trials (tree shrew). Square gratings were presented to the ferret at 0.06 cycles per degree and 4 Hz and in the tree shrew at 0.4 cycles per degree and 2 Hz. In addition, "blank" stimuli of 0% contrast were also presented. All stimuli were randomly interleaved and presented for 4s followed by 6s of gray screen (ferret) or 2s followed by 3s of gray screen (tree shrew). Timing for visual stimuli and imaging were recorded using Spike2 (v7.11b, CED; Cambridge UK).

Data analysis in the ferret was performed as previously described using custom written scripts in Python and ImageJ [35]. For both widefield and epifluorescence imaging, we corrected brain movement during imaging by maximizing phase correlation to a common reference frame. In widefield epifluorescence imaging, the ROI was drawn manually around regions where robust visually evoked activity was observed. For analysis, all images were spatially downsampled by a factor of 2 to yield 320x270 pixels. Slow drifts in fluorescence intensity were eliminated by calculating the $\Delta F/F = (F-F0)/F0$. Baseline fluorescence (F0) was calculated by applying a rank-order filter to the raw fluorescence trace (10th percentile) with a rolling time window of 60s. Responses were filtered with a spatial band-pass filter with low-pass cutoff defined as 50 μm and high-pass filter cutoff as 3200 μm. Preferred orientation was computed by taking the vector sum of the median-trial response over the stimulus period for each orientation.

For analysis, ROI were chosen semi-automatically (Cell Magic Wand v1.0) and fluorescence was computed by averaging all pixels within the ROI [26]. The $\Delta F/F$ for each ROI was computed, and F0 was calculated by applying a rank-order filter to the raw fluorescence (20th percentile) over a rolling time window (60 s). Stimulus-evoked responses were calculated as the average $\Delta F/F$ over the entire stimulus period, and orientation preferences were computed by fitting a von Mises distribution to the trial-median response for each stimulus orientation.

Data analysis and motion correction in the tree shrew was performed using custom code written in Matlab (Mathworks) or Java package for running ImageJ within Matlab (Miji). For network-level analysis, the fluorescence signal for each pixel was calculated as $\Delta F/F$, where F0 is the baseline fluorescence signal averaged over a 1 s period immediately before the start of visual stimulus, and F is the fluorescence signal averaged over the period of the stimulus. Responses to the stimulus set were fitted with a Gaussian to determine the preferred orientation and generate a pixel-based orientation preference map. For analysis at the neuronal level, regions of interest (ROIs) corresponding to visually identified neurons were drawn manually using ImageJ. The fluorescence of each ROI was measured by averaging all pixels within the ROI.

5.4.3. Dual imaging experiments in Figure 9

All animal handling and experiments were performed according to the ethical guidelines of the Institutional Animal Care and Use Committee of the Yale University School of Medicine. Brain-wide expression of GCaMP6s was achieved via neonatal sinus injection of AAV9-Syn-GCaMP6s into c57/Bl6 mice, as described previously [17, 36]. After reaching adulthood (P60), the skin and fascia over the skull were removed under isoflurane anesthesia and the animal was implanted with a custom titanium headpost and a microprism (5mm per side, Tower Optics) placed over the right visual cortex in a small craniotomy, bonded with a thin layer of dental cement (Metabond, Parkell).

Imaging experiments were carried out in awake mice head-fixed over a freely-moving wheel placed under the microscope objective. Widefield calcium imaging was performed using a Zeiss Axiozoom with a PlanNeoFluar objective (1x, 0.25 NA). Epifluorescent excitation was provided by an LED bank (Spectra X Light Engine, Lumencor) strobing 395 nm and 470 nm light, for hemodynamic correction and calcium imaging, respectively [36]. Emitted light was collected via sCMOS camera (Orca-Flash V3, Hamamatsu), with images acquired at 512 x 512 pixel resolution and 10 frames per second. Data were pre-processed for hemodynamic correction and normalized to ΔF/F values as previously described 2. Functional parcellation of cortical areas was carried out using local selective spectral clustering (LSSC, [36, 37]) to obtain a time series of fluorescence signal for each parcel.

Two-photon imaging was performed using a resonant-galvo scanning microscope (MOM, Sutter Instruments) coupled to our custom air-coupled, long-working distance objective (10x, 0.5 NA). Excitation was provided by a titanium-sapphire laser (MaiTai, SpectraPhysics) tuned to 920 nm. Light was directed into the brain after being reflected 90o by the implanted prism. Emitted light was collected by a gallium arsenide-phosphide detector (Hamamatsu) with images acquired at 512 x 512 pixel resolution and 30 frames per second. Data were motion corrected using NoRMCorre [38], and regions of interest (ROIs) corresponding to single cells were manually selected, neuropil-corrected, and normalized to ΔF/F values using custom software written in Matlab (Mathworks).

We calculated cell-centered networks (CCNs) to quantify the relationship between activity in single neurons and the large-scale cortical network in the contralateral hemisphere as described previously [17]. Briefly, we evaluated the correlation coefficients between time series related to p mesoscopic parcels and n time series related to cells to obtain C, a p×n matrix. We viewed each column of C as a compact representation of synchrony between the dynamics of each cell and the dynamics of the widefield signal and then clustered these vectors using the kmeans (k=4) function in Matlab. We obtained the centroid map of each cluster as the average correlation coefficients of all cells related to a specific cluster:

We then superimposed each centroid onto the full cortex parcellation to yield the average images in Figure 9.

5.4.4. Cochlea imaging in Figure 10

Animal studies were carried out according to the protocols approved by the Institutional Animal Care and Use Committee at Stanford University (APLAC-14345). Four weeks old male mouse from Ai14tdTomato (JAX: 007908) x Myosin15Cre [39] breeding was used for cochlear hair cell imaging. The mouse was anesthetized using ketamine (100 mg/kg) and xylazine (10 mg/kg). Anesthesia level was assessed by signs of movement or withdrawal reflex before the application of supplementary anesthetic. Mouse surgery and positioning for *in vivo* cochlear imaging was performed by the method described previously [21]. *In vivo* cochlear imaging was performed using a modified commercial two-photon microscope (Ultima, Bruker) with long working distance air objectives (Cousa objective; TU Plan ELWD 20X, NA 0.4, WD 19mm, Nikon Instruments Inc.). A Ti:sapphire laser was used with wavelength 920 nm and power 30 mW (Chameleon,

Coherent Inc.). The projected images (**Fig. 10b-e**) were acquired in an apical hair cell location (8-10 kHz) by collecting z-series 40 images with 2 μm intervals.

Funding. This work was supported by the NSF (NeuroNex #1934288 and BRAIN EAGER #1450824 to SLS; 2011542 to GBS) and the NIH (NINDS R01NS091335 and NEI R01EY024294 to SLS; R01NS128079 to ITS; R01MH099045 and DP1EY033975 to MJH; R01EY022951 to JAC; EY031133 to AHM; EY011488 and EY006821 to DF; R01EY030893 to GBS; R21DC020325 and R01DC003896 to AR), the Brain Research Foundation (BRFSG-2019-05 to ITS), the Max Planck Society (to DF), and the Swartz Foundation (to HB).

Acknowledgments. We thank Special Optics for manufacturing the objective. We thank George Chen for discussing the optical design and Antonio Perez for the mechanical design at Special Optics. We thank collaborators Stephen Macknik, Tom Franken, Stephen Van Hooser, Joe Culver, and Ben Huang for early support of the project and valuable input.

Contributions. KN motivated the project, and worked with CHY and SLS to develop the specifications. CHY designed the objective, coordinated fabrication, and characterized it. YY and CHY performed the mouse imaging in Fig. 5. ITS and LA, along with CHY and YY, performed the dendritic spine and bouton imaging in Fig. 6. JTC, JB, and DF performed the ferret and tree shrew imaging in Figs. 7 and 8. AHM, HD, JAC, and MH performed the dual-imaging in Fig. 9. JK and AR performed the cochlea imaging in Fig. 10. GBS provided feedback on mechanical design, usability, and performance. CHY and SLS wrote the paper with contributions from all authors. SLS led the project.

Disclosures. The design of the objective is not patented, and it will not be patented in the future. All designs originating in this report are free for reuse, no licensing or material transfer agreements are required. Notification is not required either, but only humbly requested. SLS is a paid consultant for companies that sell optics and multiphoton microscopes. There are no other competing interests.

Data Availability Statement. The design of the objective is fully open source and full specification are detailed in this report. Data underlying the results from imaging in animals are available from the authors upon request.

Supplemental videos.

Video 1: Z-stack of *in vivo* calcium imaging. The z-plane range spans from the brain surface to the depth of 500 μm. Frame size = 1024 x 1024 pixels. Imaging power = 80 mW.

Video 2: *In vivo* calcium imaging over a 1.7 x 1.7 mm FOV. Frame rate = 15.4 frames/s. Frame size = 1536 x 1536 pixels. Imaging power = 60 mW.

References

1. B. Heider, J. L. Nathanson, E. Y. Isacoff, E. M. Callaway, and R. M. Siegel, "Two-photon imaging of calcium in virally transfected striate cortical neurons of behaving monkey," Plos One **5** (2010).
2. M. Li, F. Liu, H. F. Jiang, T. S. Lee, and S. M. Tang, "Long-term two-photon imaging in awake macaque monkey," Neuron **93**, 1049–+ (2017).
3. S. L. Macknik, R. G. Alexander, O. Caballero, J. Chanovas, K. J. Nielsen, N. Nishimura, C. B. Schaffer, H. Slovin, A. Babayoff, R. Barak, S. M. Tang, N. S. Ju, A. Yazdan-Shahmorad, J. M. Alonso, E. Malinskiy, and S. Martinez-Conde, "Advanced circuit and cellular imaging methods in nonhuman primates," J. Neurosci. **39**, 8267–8274 (2019).
4. G. B. Smith and D. Fitzpatrick, "Viral injection and cranial window implantation for in vivo two-photon imaging," High-Resolution Imaging Cell. Proteins: Methods Protoc. **1474**, 171–185 (2016).
5. E. Trautmann, D. J. O'Shea, S. Shrestha, S. Lin, S. Ryu, and K. Shenoy, "Design of an implantable artificial dural window for chronic two-photon optical imaging in non-human primates," 2015 37th Annu. Int. Conf. Ieee Eng. Medicine Biol. Soc. (Embc) pp. 7554–7557 (2015).
6. T.-W. Chen, T. J. Wardill, Y. Sun, S. R. Pulver, S. L. Renninger, A. Baohan, E. R. Schreiter, R. A. Kerr, M. B. Orger, V. Jayaraman *et al.*, "Ultrasensitive fluorescent proteins for imaging neuronal activity," Nature **499**, 295–300 (2013).
7. H. Dana, Y. Sun, B. Mohar, B. K. Hulse, A. M. Kerlin, J. P. Hasseman, G. Tsegaye, A. Tsang, A. Wong, R. Patel *et al.*, "High-performance calcium sensors for imaging activity in neuronal populations and microcompartments," Nat. methods **16**, 649–657 (2019).
8. Y. Zhang, M. Rózsa, D. Bushey, Jihong Zheng, D. Reep, Yajie Liang, G. J. Broussard, A. Tsang, Getahun Tsegaye, R. Patel, Sujatha Narayan, J. X. Lim, Rongwei Zhang, M. B. Ahrens, G. C. Turner, S. S.-H. Wang, K. Svoboda, W. Korff, E. R. Schreiter, J. P. Hasseman, I. Kolb, and L. L. Looger, "jgcamp8 fast genetically encoded calcium indicators," (2020).

9. C.-H. Yu, J. N. Stirman, Y. Yu, R. Hira, and S. L. Smith, "Diesel2p mesoscope with dual independent scan engines for flexible capture of dynamics in distributed neural circuitry," Nat. Commun. **12**, 6639 (2021).
10. J. N. Stirman, I. T. Smith, M. W. Kudenov, and S. L. Smith, "Wide field-of-view, multi-region, two-photon imaging of neuronal activity in the mammalian brain," Nat. Biotechnol. **34**, 857–+ (2016).
11. Y. Zhang and H. Gross, "Systematic design of microscope objectives. part i: System review and analysis," Adv. Opt. Technol. **8**, 313–347 (2019).
12. N. Ji, J. Freeman, and S. L. Smith, "Technologies for imaging neural activity in large volumes," Nat Neurosci **19**, 1154–64 (2016).
13. D. C. O'Shea, "Group velocity dispersion using commercial optical design programs," Appl Opt **45**, 4740–6 (2006).
14. N. Bobroff and A. E. Rosenbluth, "Evaluation of highly corrected optics by measurement of the strehl ratio," Appl. optics **31**, 1523–1536 (1992).
15. W. R. Zipfel, R. M. Williams, and W. W. Webb, "Nonlinear magic: multiphoton microscopy in the biosciences," Nat Biotechnol **21**, 1369–77 (2003).
16. T. W. Chen, T. J. Wardill, Y. Sun, S. R. Pulver, S. L. Renninger, A. Baohan, E. R. Schreiter, R. A. Kerr, M. B. Orger, V. Jayaraman, L. L. Looger, K. Svoboda, and D. S. Kim, "Ultrasensitive fluorescent proteins for imaging neuronal activity," Nature **499**, 295–300 (2013).
17. D. Barson, A. S. Hamodi, X. Shen, G. Lur, R. T. Constable, J. A. Cardin, M. C. Crair, and M. J. Higley, "Simultaneous mesoscopic and two-photon imaging of neuronal activity in cortical circuits," Nat. methods **17**, 107–113 (2020).
18. L. Yin, Y. Geng, F. Osakada, R. Sharma, A. H. Cetin, E. M. Callaway, D. R. Williams, and W. H. Merigan, "Imaging light responses of retinal ganglion cells in the living mouse eye," J. neurophysiology **109**, 2415–2421 (2013).
19. S. Charpak, J. Mertz, E. Beaurepaire, L. Moreaux, and K. Delaney, "Odor-evoked calcium signals in dendrites of rat mitral cells," Proc. Natl. Acad. Sci. **98**, 1230–1234 (2001).
20. R. P. Barretto, S. Gillis-Smith, J. Chandrashekar, D. A. Yarmolinsky, M. J. Schnitzer, N. J. Ryba, and C. S. Zuker, "The neural representation of taste quality at the periphery," Nature **517**, 373–376 (2015).
21. J. Kim and A. J. Ricci, "In vivo real-time imaging reveals megalin as the aminoglycoside gentamicin transporter into cochlea whose inhibition is otoprotective," Proc. Natl. Acad. Sci. **119**, e2117946119 (2022).
22. T. D. Visser and J. L. Oud, "Volume measurements in three-dimensional microscopy," Scanning **16**, 198–200 (1994).
23. Y. Yu, J. N. Stirman, C. R. Dorsett, and S. L. Smith, "Mesoscale correlation structure with single cell resolution during visual coding," bioRxiv p. 469114 (2019).
24. M. Pachitariu, C. Stringer, M. Dipoppa, S. Schröder, L. F. Rossi, H. Dalgleish, M. Carandini, and K. D. Harris, "Suite2p: beyond 10,000 neurons with standard two-photon microscopy," bioRxiv p. 061507 (2017).
25. I. T. Smith, L. B. Townsend, R. Huh, H. Zhu, and S. L. Smith, "Stream-dependent development of higher visual cortical areas," Nat. neuroscience **20**, 200–208 (2017).
26. D. E. Wilson, D. E. Whitney, B. Scholl, and D. Fitzpatrick, "Orientation selectivity and the functional clustering of synaptic inputs in primary visual cortex," Nat. neuroscience **19**, 1003–1009 (2016).
27. M. F. Iacaruso, I. T. Gasler, and S. B. Hofer, "Synaptic organization of visual space in primary visual cortex," Nature **547**, 449–452 (2017).
28. S. L. Smith, I. T. Smith, T. Branco, and M. Häusser, "Dendritic spikes enhance stimulus selectivity in cortical neurons in vivo," Nature **503**, 115–120 (2013).
29. T. A. Pologruto, B. L. Sabatini, and K. Svoboda, "Scanimage: flexible software for operating laser scanning microscopes," Biomed. engineering online **2**, 1–9 (2003).
30. V. A. Kalatsky and M. P. Stryker, "New paradigm for optical imaging: temporally encoded maps of intrinsic signal," Neuron **38**, 529–545 (2003).
31. J. T. Chang, D. Whitney, and D. Fitzpatrick, "Experience-dependent reorganization drives development of a binocularly unified cortical representation of orientation," Neuron **107**, 338–350 (2020).
32. K.-S. Lee, X. Huang, and D. Fitzpatrick, "Topology of on and off inputs in visual cortex enables an invariant columnar architecture," Nature **533**, 90–94 (2016).
33. A. Edelstein, N. Amodaj, K. Hoover, R. Vale, and N. Stuurman, "Computer control of microscopes using μmanager," Curr. protocols molecular biology **92**, 14–20 (2010).
34. J. W. Peirce, "Psychopy—psychophysics software in python," J. neuroscience methods **162**, 8–13 (2007).
35. J. T. Chang and D. Fitzpatrick, "Development of visual response selectivity in cortical gabaergic interneurons," Nat. Commun. **13**, 1–14 (2022).
36. S. Lohani, A. H. Moberly, H. Benisty, B. Landa, M. Jing, Y. Li, M. J. Higley, and J. A. Cardin, "Dual color mesoscopic imaging reveals spatiotemporally heterogeneous coordination of cholinergic and neocortical activity," BioRXiv pp. 2020–12 (2021).
37. G. Mishne, R. R. Coifman, M. Lavzin, and J. Schiller, "Automated cellular structure extraction in biological images with applications to calcium imaging data," BioRXiv p. 313981 (2018).
38. E. A. Pnevmatikakis and A. Giovannucci, "Normcorre: An online algorithm for piecewise rigid motion correction of calcium imaging data," J. neuroscience methods **291**, 83–94 (2017).
39. E. Caberlotto, V. Michel, I. Foucher, A. Bahloul, R. J. Goodyear, E. Pepermans, N. Michalski, I. Perfettini, O. Alegria-Prévot, S. Chardenoux *et al.*, "Usher type 1g protein sans is a critical component of the tip-link complex, a structure controlling actin polymerization in stereocilia," Proc. Natl. Acad. Sci. **108**, 5825–5830 (2011).